Article

Plasma-Treated Cobalt-Doped Nanoporous Graphene for Advanced Electrochemical Applications

Florian Knabl [1,*], Nikolaos Kostoglou [1,*], Ram K. Gupta [2], Afshin Tarat [3], Steven Hinder [4], Mark Baker [4], Claus Rebholz [1,5] and Christian Mitterer [1]

1 Department of Materials Science, Montanuniversität Leoben, 8700 Leoben, Austria; claus@ucy.ac.cy (C.R.); christian.mitterer@unileoben.ac.at (C.M.)
2 Department of Chemistry, Pittsburg State University, Pittsburg, KS 66762, USA; rgupta@pittstate.edu
3 Loginns GmbH, 9020 Klagenfurt, Austria
4 Department of Mechanical Engineering Sciences, University of Surrey, Guildford GU2 7XH, UK; s.hinder@surrey.ac.uk (S.H.); m.baker@surrey.ac.uk (M.B.)
5 Department of Mechanical and Manufacturing Engineering, University of Cyprus, Nicosia 1678, Cyprus
* Correspondence: florian.knabl@unileoben.ac.at (F.K.); nikolaos.kostoglou@unileoben.ac.at (N.K.)

Abstract: Metal–carbon nanocomposites are identified as key contenders for enhancing water splitting through the oxygen evolution reaction and boosting supercapacitor energy storage capacitances. This study utilizes plasma treatment to transform natural graphite into nanoporous few-layer graphene, followed by additional milling and plasma steps to synthesize a cobalt–graphene nanocomposite. Comprehensive structural characterization was conducted using scanning and transmission electron microscopy, X-ray diffraction, Raman spectroscopy, gas sorption analysis and X-ray photoelectron spectroscopy. Electrochemical evaluations further assessed the materials' oxygen evolution reaction and supercapacitor performance. Although the specific surface area of the nanoporous carbon decreases from 780 to 480 m^2/g in the transition to the resulting nanocomposite, it maintains its nanoporous structure and delivers a competitive electrochemical performance, as evidenced by an overpotential of 290 mV and a Tafel slope of 110 mV/dec. This demonstrates the efficacy of plasma treatment in the surface functionalization of carbon-based materials, highlighting its potential for large-scale chemical-free application due to its environmental friendliness and scalability, paving the way toward future applications.

Keywords: graphene; plasma; cobalt; nanocomposites; nanoporous powders; water splitting; oxygen evolution reaction; supercapacitor

1. Introduction

The ever-increasing global demand for energy, coupled with the climate crisis from emissions of carbon dioxide and other greenhouse gases, underscores the urgent need for solutions to ensure a more sustainable future. Significant efforts are underway to develop materials that facilitate efficient and environmentally friendly energy conversion and storage. Hydrogen, as a clean energy carrier synthesized ideally through water electrolysis, holds promise for a sustainable future. Electrolytic water splitting, encompassing both the hydrogen evolution reaction (HER) and the oxygen evolution reaction OER) [1], requires an effective catalyst to enhance kinetics and cost-effectiveness. Meanwhile, supercapacitors are considered to be another important cornerstone of advanced clean energy technologies. They offer substantial power densities for energy storage and rapid charging and discharging, utilizing the formation of electric double layers and electrochemical pseudocapacitance [2].

Carbon-based nanoporous materials are prime candidates for both OER [3] and supercapacitor applications [4,5] due to their superior properties, such as high chemical and mechanical stability, excellent electrical conductivity and expansive specific surface

areas with adjustable pore size distributions. Enhancing these intrinsic properties through surface functionalization is a key area of current research [6], offering the potential for even more optimized performance in energy-related applications. Cobalt nanoparticles [7] and cobalt oxides [8] have been used for the OER in previous studies, with multiple reports on bimetallic and mixed oxide systems containing cobalt listed in [9]. Multiple studies investigated cobalt-based materials for supercapacitor applications [10].

Nanocomposites that integrate carbon with cobalt present an attractive approach toward harnessing the beneficial properties of both constituents and potentially achieving synergistic effects. Multiple cobalt-doped graphitic materials were investigated with respect to their OER performance, including cobalt-embedded nitrogen-doped carbon nanotubes [11,12], as well as composites containing porous carbons [13,14]. Supercapacitor applications of cobalt oxide with graphene nanosheets were presented by Naveen et al. [15] and Lakra et al. [16]. Furthermore, Liu et al. [17] designed a composite using mesoporous carbon nanospheres decorated with cobalt-based nanoparticles that showed enhanced supercapacitor performance, demonstrating ongoing research in those topics.

The graphene-based materials discussed in the literature are synthesized using a variety of methods, such as the mechanical exfoliation of graphite [18], the reduction of graphene oxide [19] and chemical-vapor-deposition-based synthesis [20], among others [21,22]. However, purely physical techniques like plasma-assisted exfoliation of natural graphite are rarely employed. Our previous work pioneered this approach, transforming natural graphite into nanoporous few-layer graphene (FLG) with a markedly high specific surface area that was used for hydrogen storage [23], followed by a study on water purification and supercapacitor performance [24]. Hence, this method not only highlights the potential for a more efficient synthesis process but also suggests improved performance characteristics for energy-related applications.

In this work, we introduce an innovative approach by implementing an additional plasma-processing step after mixing FLG with cobalt powder, yielding cobalt-enriched few-layer graphene (Co-FLG). This composite is compared to its pure FLG counterpart through a series of structural and electrochemical characterization methods, including scanning electron microscopy (SEM), energy-dispersive X-ray spectroscopy (EDX), transmission electron microscopy (TEM), X-ray diffraction (XRD), Raman spectroscopy, gas sorption analysis (GSA) and X-ray photoelectron spectroscopy (XPS). The electrochemical analyses specifically assess the oxygen evolution reaction and supercapacitor performances. This study marks the first demonstration that a purely physical method can effectively create carbon–cobalt composite materials exhibiting enhanced electrochemical performance compared to the pure nanoporous graphene. The method stands out for its dry/chemical-free, cost-efficient and environmentally friendly character, presenting a scalable solution for industry. The findings of this study not only advance the understanding of metal–carbon composites but also open new avenues for the development of green energy technologies based on these novel materials.

2. Materials and Methods

2.1. Material Synthesis

The FLG material was synthesized by subjecting natural flake graphite (Asbury Carbons, Ashbury, NJ) to plasma treatment using a multi-electrode dielectric barrier discharge plasma reactor, operating under the conditions outlined in [23]. The graphite was subjected to an argon flow of 600 sccm (corresponding to a pressure of 0.1 mbar) with a power of 6 kW for 60 min. Following this, the resultant FLG powder underwent a further 30 min oxygen plasma treatment to add oxygen-containing functional groups aimed at decreasing particle agglomeration.

A total of 100 g of the FLG material was then mixed with 5 g of cobalt powder (Thermo Scientific Chemicals, Waltham, MA, USA) of 99.8% purity and a 1.6 μm average particle size, using mechanical stirring for 5 min to ensure uniformity. This mixture was then subjected to an additional argon plasma treatment step for 60 min within the same reactor using the same

gas flow and power values as above. These specific conditions/process parameters were determined in preliminary studies and were chosen to promote the uniform distribution of cobalt particles within the FLG matrix and to optimize the composite's physical and electrochemical characteristics.

2.2. Structural and Morphological Characterization

The SEM micrographs were collected by an FEI Quanta 200 microscope (Hillsboro, OR, USA) using a 20 kV acceleration voltage and a working distance of 10 mm. EDX elemental maps were collected with an EDVAC Genesis X-ray analysis probe mounted on the SEM instrument using the same 20 kV acceleration voltage.

The TEM micrographs were recorded by employing a Philips CM-20 (Eindhoven, Netherlands) transmission electron microscope with high-resolution capabilities equipped with a LaB_6 filament and operated at 200 kV acceleration voltage. The powders were first ultra-sonicated in ethanol and then placed onto holey carbon-only support films mounted on copper grids.

The XRD investigations were performed on a Bruker-AXS D8 Advance diffractometer (Karlsruhe, Germany) in a Bragg–Brentano configuration. The diffractograms were recorded using Cu Kα radiation with a wavelength of ~0.154 nm operating with a voltage of 40 kV and a current of 40 mA. The scans were recorded from diffraction angles of 15°–60° in a continuous scan mode with a step size of 0.02° and a time of 1.2 s per step. Bragg's law was used to calculate the interplanar spacing d between the individual graphene layers from the (002) reflection. Scherrer's equation was used to calculate the crystallite size L_c from the (002) reflection [25]. The number of graphene layers n was estimated by dividing the L_c value by the d value ($n = L_c/d$).

Micro-Raman spectroscopy was conducted utilizing an inVia Reflex spectrometer (Renishaw, Wotton-under-Edge, UK), equipped with a 514.5 nm solid-state laser for excitation. The laser beam, focused to a 4.5 mm diameter spot, was directed through an objective lens featuring ×20 magnification and a numerical aperture of 0.14. A power density of 0.02 W/μm^2, following guidelines from a prior study [26], was applied.

The GSA studies were performed on an Autosorb iQ^3 gas sorption analyzer (Anton Paar QuantaTec, Boynton Beach, FL, USA) using high-purity (99.999%) N_2 and He gases for the adsorption measurements and void volume calculations, respectively, with liquid N_2 at 77 K as a cryogen. The samples (~50 mg) were degassed at 250 °C under vacuum for 24 h prior to performing the GSA measurements. To determine the specific surface area, the multi-point Brunauer–Emmett–Teller (BET) method [27] was utilized, adhering to the BET consistency criteria outlined in ISO 9277:2022. This calculation was based on adsorption data at relative pressures (P/P_0) ranging from 0.01 to 0.05. The values for the micropore surface area and micropore volume were calculated using the t-plot method for carbon black in the relative pressure (P/P_0) interval from 0.2 to 0.5. The pore size distributions were estimated using the quenched solid density functional theory (QSDFT). This method employed the N_2–carbon adsorption branch kernel at 77 K for analyzing mixed slit and cylindrical pores.

The XPS analysis was conducted on a Theta Probe system (Thermo Scientific, Waltham, MA, USA) featuring a monochromated Al Kα X-ray source with 1486.6 eV photon energy. The X-ray spot was focused to approximately 400 μm in diameter. The wide-scan survey spectra were collected at a pass energy of 200 eV, and the high-resolution core level spectra for various elements were obtained with a pass energy of 50 eV.

### 2.3. Electrochemical Characterization

The electrochemical properties were assessed using a three-electrode configuration in a 1 M KOH solution (pH value 13.89–14.06 [28]) for a catalytic activity analysis (using OER) and a 3 M KOH solution (pH value 14.56–14.74 [28]) for the energy storage studies (using supercapacitors). The setup consisted of a saturated calomel electrode as the reference, a platinum wire as the counter and custom-made electrodes as the working electrodes. These

electrodes were fabricated by blending 80 wt.% FLG or Co-FLG with 10wt.% acetylene black and 10 wt.% polyvinylidene difluoride in N-methyl pyrrolidinone, applied onto nickel foam substrates with a total working electrode area of 0.25 cm^2. For the OER studies, linear sweep voltammetry (LSV) and a Tafel slope analysis were employed to assess the kinetics and efficiency of the catalytic process. For evaluating the supercapacitive behavior, cyclic voltammetry (CV) and long-term durability tests, extending over 5000 cycles, were performed to assess the charge storage efficiency and electrode stability. These tests were conducted using a VersaSTAT 4-500 electrochemical workstation (Princeton Applied Research, Oak Ridge, TN, USA), allowing for a comprehensive analysis of both the catalytic activity and energy storage capabilities.

3. Results and Discussion

### 3.1. Structural and Morphological Investigations

The field-emission SEM micrographs of both the FLG and Co-FLG samples reveal a mix of individual spherical particle agglomerates, with sizes typically below 1 μm in diameter, at lower magnifications (Figure 1a,d). At higher magnifications (Figure 1b,e), a platelet-like structure is visible. The high-resolution TEM micrographs of the FLG (Figure 1c) reveal individual thin flakes with various structural defects. In contrast, the Co-FLG TEM micrographs (Figure 1f) display a mixture of carbon flakes and spherical particles, the latter appearing darker and indicating cobalt's presence. The EDX analysis of the FLG identifies a high oxygen content alongside carbon, indicative of successful functionalization. For the Co-FLG sample, EDX confirms the presence of cobalt. The EDX mappings of the spherical agglomerates were conducted for carbon (Figure 1g), oxygen (Figure 1h) and cobalt (Figure 1i), revealing that carbon is uniformly distributed throughout the sample, while cobalt is significantly less predominant and concentrated along specific surface sites of the sample.
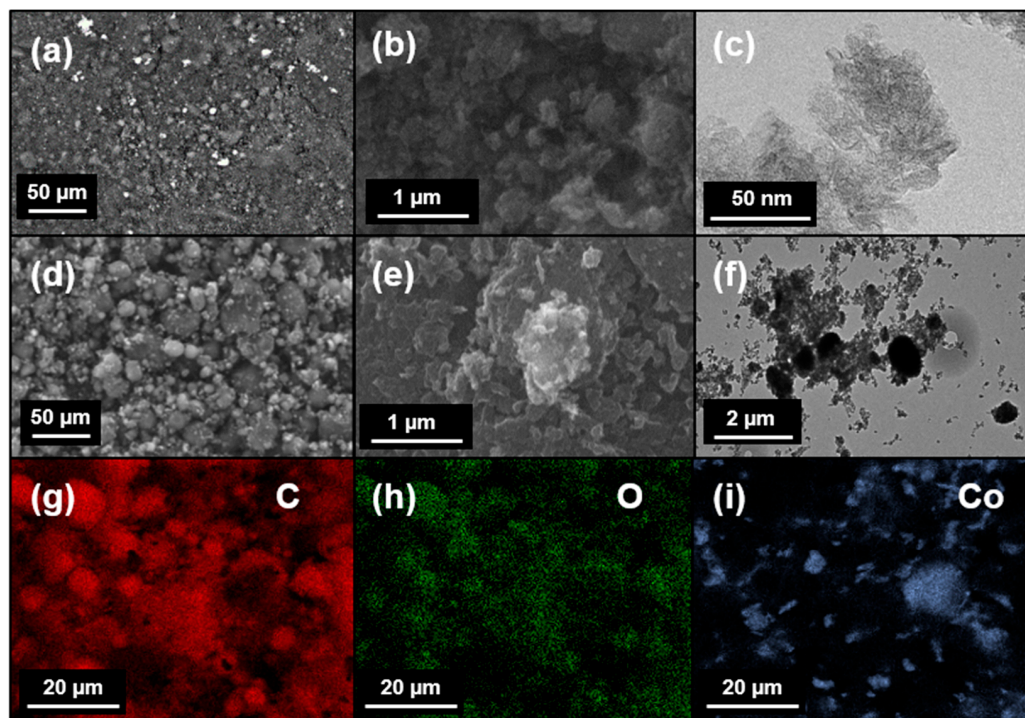
Figure 1. (**a**,**b**) SEM and (**c**) TEM micrographs for FLG. (**d**,**e**) SEM and (**f**) TEM micrographs for Co-FLG. EDX mappings of Co-FLG for (**g**) carbon, (**h**) oxygen and (**i**) cobalt.

XRD experiments were conducted, with the diffractograms depicted in Figure 2a. The FLG sample reveals a distinct (002) peak at a diffraction angle 2θ of 26.3° and a broad (100) peak located around 43.3°, both associated with the graphitic structure (International

Centre for Diffraction Data card no. 75-1621). The Co-FLG sample reveals graphitic peaks as well as strong contributions attributed to both the face-centered cubic (fcc) and hexagonal close-packed (hcp) phases of cobalt. While the hcp phase is thermodynamically stable at room temperature, the two phases are known to coexist at room temperature [29]. Notably, there are no peaks indicating the presence of cobalt oxides (i.e., CoO and Co_3O_4) in the XRD patterns. Applying Bragg's law, the interplanar spacing d between the individual graphene layers is calculated as 0.338 nm for both samples, slightly higher than the theoretical graphite interlayer spacing of 0.335 nm [30]. Applying Scherrer's equation allows for calculating the crystallite size L_c of 5.7 and 5.4 nm and correspondingly an average number of layers of ~17 and 16 layers for the FLG and Co-FLG, respectively. The striking similarities between both samples imply that the additional plasma treatment step does not cause significant structural changes to the carbon phase of the Co-FLG sample.
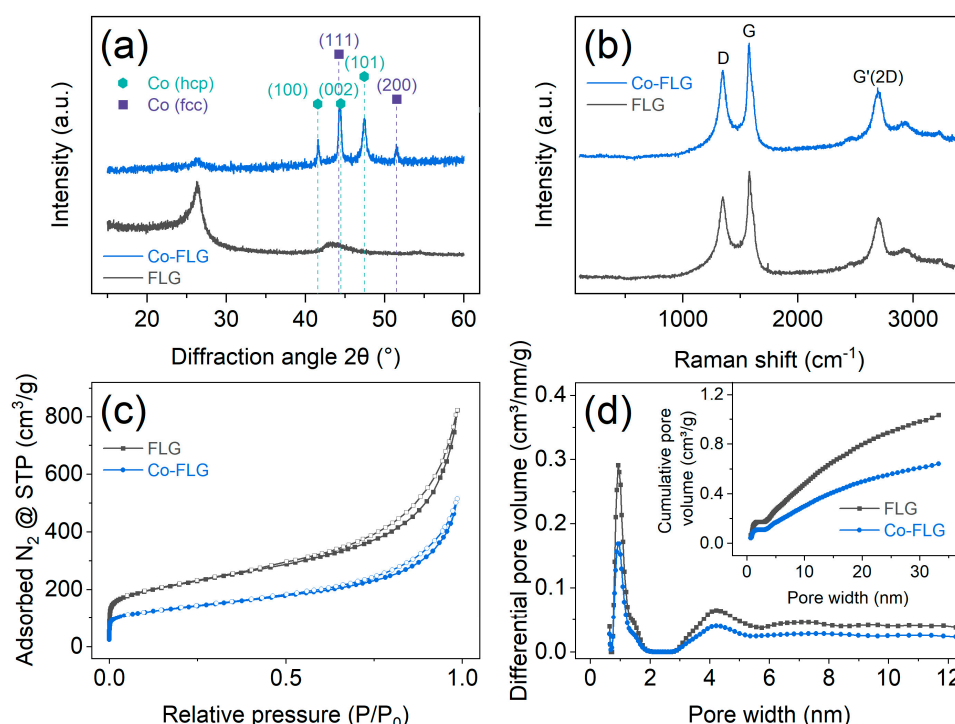
Figure 2. Results of structural characterization of FLG (black) and Co-FLG (blue): (**a**) X-ray diffractograms with the positions of the main diffraction peaks of the allotropic fcc and hcp phases of cobalt and (**b**) Raman spectra with indications for the D, G and G'(2D) bands. (**c**) Gas adsorption/desorption isotherms for N_2 at 77 K and corresponding (**d**) QSDFT-derived pore size distributions with an inset showing the cumulative pore volume.

Raman spectroscopy was conducted and the results are shown in Figure 2b, revealing three distinct features known as the D, G and G'(2D) bands of carbons [31] located at 1353, 1576 and 2695 cm^{-1}, respectively. All the peak positions and integrated peak areas are virtually identical for both samples, with the presence of a strong D band suggesting a high defect density in the carbon structure. The shape and position of the G'(2D) band indicates a graphene-based structure with a few layers, rather than graphite [32]. The extensive similarities between both Raman spectra suggest that the incorporation of cobalt does not alter the carbon structure. The anticipated peaks for the cobalt oxides, which would typically appear at 690 cm^{-1} for Co_3O_4 [33] and a broad band around 1060 cm^{-1} for CoO [34,35], are absent, supporting the findings from the XRD. The defect density is calculated for both samples as ~1.88×10^{11} cm^{-2} following a procedure outlined by Cançado et al. [36]. The results of this investigation show that no significant structural evolution of the nanoporous graphene phase was found after conducting the second plasma treatment step.

The results of the gas sorption analysis are depicted in Figure 2c,d. Figure 2c shows the gas adsorption (filled symbols) and desorption (empty symbols) isotherms using N_2 at 77 K. The sharp increase at low relative pressures can be attributed to microporosity (i.e., pore widths below 2 nm). The isotherms are similar in shape, with the FLG sample displaying a significantly higher N_2 adsorption amount throughout the full pressure range. For the concluding point of the adsorption isotherms ($P/P_0 \sim 0.99$), the Co-FLG exhibits a reduced N_2 adsorption of roughly 37% compared to the FLG. The desorption branch for both samples shows a small hysteresis, indicating the presence of mesopores (i.e., pore widths between 2 and 50 nm). The adsorption isotherms do not end with a plateau; thus, the Gurvich rule cannot be applied to determine the total pore volume [37]. The isotherms are classified as a mixed Type I and Type IV(a) according to the classification of the International Union of Pure and Applied Chemistry, as both a contribution from the micropores in the low pressure range and the mesopores in the intermediate pressure range is visible [38]. A small step-down in the desorption branch in the P/P_0 range between 0.5 and 0.4 is visible for both samples. This is commonly reported in the literature and is attributed to cavitation-induced N_2 evaporation from the mesopores [37,39]. Thus, the adsorption branch is used for extracting the pore size distribution depicted in Figure 2d. Using the desorption branch would yield an artifact in the pore size distribution in the range between 3 and 4 nm, associated with the cavitation-induced evaporation mechanism [39]. The pore size distribution for both samples is virtually identical, exhibiting a bimodal distribution with peaks at 0.93 and 4.22 nm, thus revealing super-micropores (i.e., pore widths between 0.7 and 2 nm) and small mesopores, respectively. It seems that there are no pores in the size range of 2 to 2.8 nm present within the investigated samples. The inset in Figure 2d reveals the cumulative pore size distribution for both samples. The BET method reveals apparent surface areas of 780 m^2/g for the FLG and 484 m^2/g for the Co-FLG, which corresponds to a reduction of roughly 38% upon cobalt addition. The t-plot method was employed to extract the micropore surface area and the micropore volume of the given samples. The overall contribution of the micropores is roughly 35% for both samples. The remaining surface area S_{ext} consists of contributions from mesopores, macropores and the external surface. However, a more precise quantification cannot be performed, as the isotherm lacks a plateau in the high-pressure range. Consequently, no mean pore width value can be reported. The results of the GSA are summarized in Table 1. To conclude, both samples show a virtually identical pore size distribution, while Co-FLG displayed a decrease of roughly 38% with respect to both the specific surface area and the micropore volume. This effect is attributed to pore blocking, as previously described in literature [26].

Table 1. Results of the gas sorption analysis conducted using N_2 at 77 K.

Material	S_{BET} [m^2/g]	S_{micro} [m^2/g]	S_{ext} [m^2/g]	V_{micro} [cm^3/g]
FLG	780	279	501	0.123
Co-FLG	484	175	309	0.077
Change	−37.9%	−37.3%	−38.4%	−37.4%

S_{BET}: Brunauer–Emmett–Teller (BET) specific surface area. S_{micro}: Specific surface area calculated by the statistical thickness t-plot method. S_{ext}: Specific surface area contributed by mesopores, macropores and external surfaces, calculated as difference between S_{BET} and S_{micro}. V_{micro}: Specific micropore volume calculated by the t-plot method.

XPS measurements were performed to analyze the elemental composition of the samples. Figure 3a presents the wide-scan survey spectra, showing carbon and oxygen in both samples and additionally cobalt in the Co-FLG. A quantitative analysis from the survey scans determines the chemical compositions to be 94.1 and 91.9 at.% of carbon, 5.6 and 6.7 at.% of oxygen, small quantities of nitrogen (0.3 and 0.6 at.%) for the FLG and Co-FLG, respectively, and 0.8 at.% of cobalt for the Co-FLG. This translates to 3.3 wt.% of cobalt, which is slightly lower than the anticipated 4.8 wt.% based on the synthesis procedure.
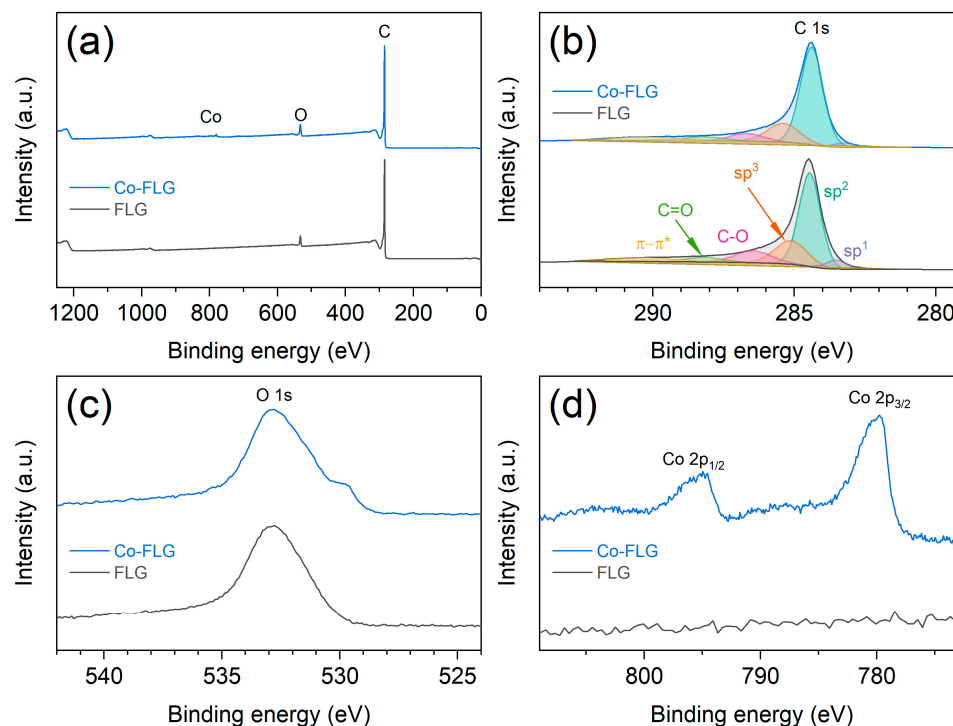
Figure 3. Results of XPS investigations on FLG (black) and Co-FLG (blue) consisting of a (**a**) survey scan and high-resolution spectra for the elements (**b**) carbon, (**c**) oxygen and (**d**) cobalt.

Figure 3b displays the high-resolution spectra of carbon, where the peak deconvolution reveals the presence of sp^1, sp^2, sp^3, C-O and C=O bonds, along with a π-π^* satellite peak in the 290–292 eV region [40]. The spectra are predominantly characterized by sp^2-hybridized carbon bonds associated with the peak position at 284.5 eV, which represent the largest fraction of the carbon content, accounting for ~56% in both examined samples. Contributions from sp^3-hybridized carbon are also significant, comprising ~21% and ~16% for the FLG and Co-FLG samples, respectively, with small contributions from the remaining carbon bonds.

High-resolution oxygen spectra are depicted in Figure 3c, with a peak shape indicative of the presence of OH^- species and adsorbed H_2O. The additional peak at low binding energies corresponds to cobalt oxide formation [41]. Figure 3d confirms cobalt's presence in the Co-FLG, in good agreement with the EDX-derived elemental map for cobalt (see Figure 1i). The Co $2p_{3/2}$ peak occurs at a binding energy of 779.8 eV. This binding energy together with only a weak satellite structure at around 790 eV between the $2p_{3/2}$ and $2p_{1/2}$ peaks is characteristic of Co_3O_4, [41–43], as expected for the native oxide [41]. Based on the theoretical work, cobalt and cobalt oxides are expected to transform into CoOOH under the conditions present during an OER [44].

The incorporation of cobalt into the FLG, as indicated by Figures 1i, 2a and 3d, leaves the carbon structure unaltered, as evidenced by the Raman spectroscopy and gas sorption analyses. The TEM observations reveal mostly spherical cobalt particles, with their presence further validated by EDX mapping, XRD and XPS. The overall pore size distribution remains consistent despite the cobalt addition. However, a notable reduction in the specific surface area by 38% is observed. The incorporation of cobalt might enable tuning the material's functionality. In the next step, the electrochemical performance differences between FLG and Co-FLG were investigated by means of OER and supercapacitor energy storage applications.

3.2. Electrochemical Characterization

The electrochemical performance of FLG and Co-FLG in terms of the OER was analyzed using LSV, as shown in Figure 4a. As the potential increases, the current density for both materials also increases, which is typical for catalytic processes, as the overpotential provides additional driving force for the reactions. Notably, the Co-FLG exhibits a higher current density than the FLG at potentials beyond approximately 1.55 V, suggesting that cobalt doping enhances the electrocatalytic activity of the graphene material. At a benchmark current density of 10 mA/cm^2, overpotentials of 280 mV for FLG and 290 mV for Co-FLG are observed, comparable to the 300 mV/cm^2 reported by Dou et al. [13] for a porous carbon doped with cobalt nanoparticles in 0.1 M KOH media and mirroring the 290 mV/cm^2 reported by Jia et al. [45] for cobalt nanoparticles embedded in nitrogen-doped carbon on carbon cloth in a 1 M KOH solution.
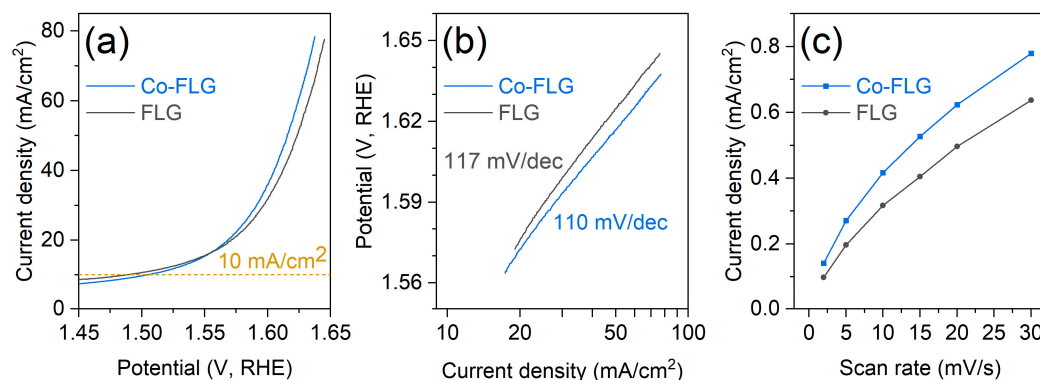
Figure 4. Characterization of OER performance. (**a**) LSV curves, (**b**) corresponding Tafel slopes and (**c**) current density as a function of the scan rate.

A further analysis of the OER kinetics reveals that Co-FLG has a lower Tafel slope (110 mV/dec) compared to FLG (117 mV/dec), as seen in Figure 4b. This suggests that Co-FLG requires a smaller increase in potential to achieve a tenfold increase in current density compared to FLG, which indicates that Co-FLG has a better catalytic efficiency for the OER. The lower Tafel slope of the Co-FLG sample indicates a higher electrocatalytic surface area. The Tafel slope of 117 mV/dec for the FLG sample implies that an electrochemical step is determining the rate-limiting step rather than chemical reactions based on the theoretical works [46,47]. For the case of Co-FLG, the reported Tafel slope of 110 mV/dec is not directly covered by the theoretical calculations in the literature, which also applies for subsequent experimentally derived Tafel slope values. Jia et al. reported various Tafel slopes of 73 and 88 mV/dec for two different types of N-doped carbon cloth materials also doped with cobalt and 253 mV/dec for the N-doped carbon cloth without cobalt addition under a 1 M KOH solution. The synthesis procedure consisted of electrochemically deposited Co$_3$O$_4$ nanosheets on the carbon cloth surface [45]. Dou et al. reported a significantly lower Tafel slope of 96.9 mV/dec for a cobalt nanoparticle-doped porous carbon and a lower Tafel slope of 73 mV/dec for a more advanced material system incorporating carbon nanotubes [13], however with no reasons given for the differences in the Tafel slopes. It has to be noted that the cobalt nanoparticles were significantly smaller compared to this work and a 0.1 M KOH solution was used. Mao et al. reported on 3D crumpled graphene–cobalt oxide nanohybrids with an overpotential of 340 mV at 10 mA/cm^2 and Tafel slopes of 71 and 75 mV/dec for N-doped and non-doped versions of the material system [48]. Su et al. reported Tafel slopes between 61.4 and 116.1 mV/dec for cobalt nanoparticles embedded in N-doped carbon with values depending on different synthesis parameters of the material system [49].

The current density was studied as a function of the scan rate (see Figure 4c). Co-FLG is characterized by consistently higher current densities compared to FLG, culminating in a

22% higher current density at the highest tested scan rate of 30 mV/s. This enhancement in electrochemical activity underscores Co-FLG's potential for high-current-density applications.

To summarize, the presented material system is capable of achieving a competitive overpotential at 10 mA/cm^2 while only obtaining intermediate Tafel slopes. The material system could be further enhanced by N-doping the few-layer graphene [3]. This could be performed within the plasma reactor using an additional plasma treatment step with nitrogen gas.

Figure 5a presents a comparative evaluation of the specific capacitance as a function of the current density for FLG and Co-FLG in supercapacitor applications. Both curves exhibit a decrease in specific capacitance with increasing current density. At a current density of 0.5 A/g, FLG achieves a significantly higher specific capacitance (125.8 F/g) compared to Co-FLG (99.6 F/g), marking a 26% increase. The specific capacitance of FLG decreases significantly with the current density, achieving roughly equal values of 62 F/g at 3 A/g compared to Co-FLG and terminating with 3.6 F/g at the highest measured current density of 20 A/g. In contrast, Co-FLG retains a significantly higher specific capacitance at elevated current densities, i.e., 24.6 F/g at 20 A/g, thus outperforming the conventional FLG by a factor of 6.8. The results for the specific capacitance as a function of the scan rate are depicted in Figure 5b. In a similar fashion to Figure 5a, Co-FLG starts at a lower specific capacitance at low scan rates and outperforms the FLG at higher scan rates, despite a less pronounced difference of 27%. This indicates that Co-FLG might be particularly useful for applications requiring rapid charge–discharge cycles, where maintaining the energy storage capacity is crucial. Benchmarking the performance of supercapacitors is complex, as standardized benchmarks, similar to those for the OER, are absent. Lu et al. addressed this complexity in their recent review, showcasing a range of cobalt-based graphene materials [50]. The Co$_3$O$_4$/graphene nanosheets composite prepared by Naveen et al. performed significantly better with 175 F/g at 10 A/g in a 1 M KOH solution (compared to 37.9 F/g for Co-FLG) and with 650 F/g at 5 mV/s (compared to 283 F/g for Co-FLG) in a 1 M KOH solution [15]. Dong et al. reported on a 3D graphene foam–cobalt oxide nanowire electrode achieving 768 F/g at a current density of 10 A/g (compared to 38 F/g for Co-FLG) combined with outstanding cycling stability [51]. Yan et al. reported on a similar nanocomposite synthesized using a plasma-assisted process, achieving 243 F/g at 5 mV/s (compared to 236.7 F/g for Co-FLG) in a 6 M KOH aqueous solution [52].
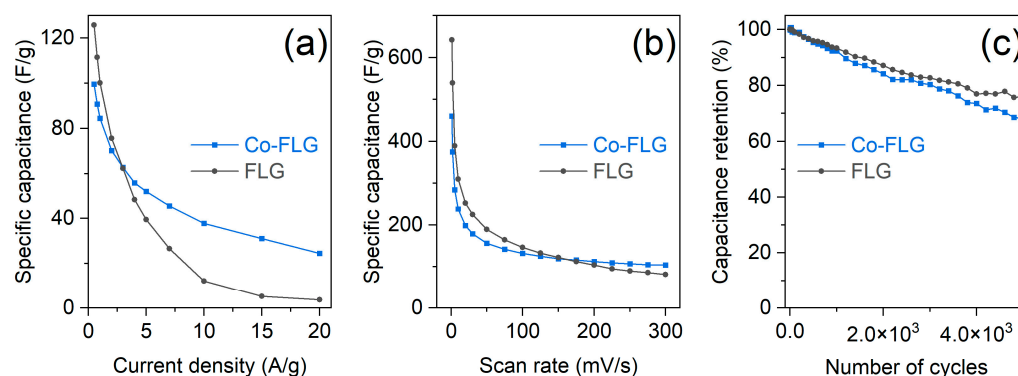
Figure 5. Supercapacitor performance. (**a**) Specific capacitance as a function of the current, (**b**) specific capacitance as a function of the scan rate and (**c**) capacitance retention over 5000 cycles.

When the specific capacitance is normalized by the BET specific surface area, yielding values in F/m^2, Co-FLG consistently outperforms FLG. At a current density of 0.5 A/g, Co-FLG achieves a notable specific capacitance of ~0.21 F/m^2, compared to ~0.16 F/m^2 for FLG. This performance gap widens with increasing current densities; at the highest tested current density of 20 A/g, Co-FLG exceeds FLG by a factor of 11, demonstrating specific capacitances of ~0.051 and ~0.005 F/m^2, respectively. This underlines the enhanced

electrochemical performance achieved by the addition of cobalt despite the reduction in the available surface area.

The cycling stability tests (Figure 5c) reveal a gradual decline in capacitance retention for both Co-FLG and FLG over 5000 cycles. FLG performs more favorably, retaining 76% of its original capacitance, while Co-FLG retains 68% after 5000 cycles. The lower capacitance retention of Co-FLG indicates more pronounced degradation from cycling, potentially due to microstructural changes, or the instability of cobalt dopants. Yan et al. reported a slight increase in cyclic capacitance for their nanocomposite within the first 250 cycles and a subsequent decrease to 95% after a total of 2000 cycles, compared to 84% for Co-FLG and 87% for FLG [52]. Vilian et al. reported a retention of 80.5% after 5000 cycles for hexagonal Co_3O_4-anchored reduced graphene oxide sheets [53]. Liu et al. reported an excellent cycling retention of 96% after 5500 cycles for a material system consisting of hierarchical porous carbon frameworks containing ultrafine metallic cobalt nanoparticles [17]. Naveen et al. reported a cycling retention of 92% after 1000 cycles, matching the performance of Co-FLG [15]. Assessing cycling stability suffers from non-uniform testing conditions and the reasons for degradation are rarely discussed within the literature.

To summarize, Co-FLG enhances the supercapacitor performance of the given FLG material and delivers reasonable performance while falling short of matching the best currently available materials. Further optimization of the sample morphology and the length scale of the cobalt phase is suggested to further enhance supercapacitor performance [50]. It has to be noted that the presented performance was achieved by means of physical methods only, thus allowing for a wet-free synthesis procedure, with no comparable results yet published to the best of the authors' knowledge.

4. Conclusions

Within this work, we pioneered the synthesis of a nanocomposite of cobalt and nanoporous graphene synthesized by purely physical plasma treatment methods without the need for chemicals and cobalt precursors. We demonstrated for the first time that such processes can be successfully employed to obtain innovative material systems with a competitive oxygen evolution reaction and supercapacitor performance while retaining the advantageous properties of nanoporous graphene. However, the presented method does not yet allow for achieving an electrochemical performance on the same level as the best cobalt–carbon nanocomposites available in the literature. Looking forward, the incorporation of nitrogen into the carbon structure via plasma treatment processes emerges as a potential area for further research, promising to further optimize electrochemical performance.

References

1. Jiao, Y.; Zheng, Y.; Jaroniec, M.; Qiao, S.Z. Design of electrocatalysts for oxygen- and hydrogen-involving energy conversion reactions. *Chem. Soc. Rev.* **2015**, *44*, 2060–2086. [CrossRef] [PubMed]
2. Bueno, P.R. Nanoscale origins of super-capacitance phenomena. *J. Power Sources* **2019**, *414*, 420–434. [CrossRef]
3. Zhang, L.; Xiao, J.; Wang, H.; Shao, M. Carbon-Based Electrocatalysts for Hydrogen and Oxygen Evolution Reactions. *ACS Catal.* **2017**, *7*, 7855–7865. [CrossRef]
4. Pandolfo, A.G.; Hollenkamp, A.F. Carbon properties and their role in supercapacitors. *J. Power Sources* **2006**, *157*, 11–27. [CrossRef]
5. Zhai, Z.; Zhang, L.; Du, T.; Ren, B.; Xu, Y.; Wang, S.; Miao, J.; Liu, Z. A review of carbon materials for supercapacitors. *Mater. Des.* **2022**, *221*, 111017. [CrossRef]
6. Wen, Z.; Wang, X.; Mao, S.; Bo, Z.; Kim, H.; Cui, S.; Lu, G.; Feng, X.; Chen, J. Crumpled Nitrogen-Doped Graphene Nanosheets with Ultrahigh Pore Volume for High-Performance Supercapacitor. *Adv. Mater.* **2012**, *24*, 5610–5616. [CrossRef] [PubMed]
7. Wu, L.; Li, Q.; Wu, C.H.; Zhu, H.; Mendoza-Garcia, A.; Shen, B.; Guo, J.; Sun, S. Stable Cobalt Nanoparticles and Their Monolayer Array as an Efficient Electrocatalyst for Oxygen Evolution Reaction. *J. Am. Chem. Soc.* **2015**, *137*, 7071–7074. [CrossRef]
8. Zhang, Y.; Ouyang, B.; Xu, J.; Jia, G.; Chen, S.; Rawat, R.S.; Fan, H.J. Rapid Synthesis of Cobalt Nitride Nanowires: Highly Efficient and Low-Cost Catalysts for Oxygen Evolution. *Angew. Chem. Int. Ed.* **2016**, *55*, 8670–8674. [CrossRef] [PubMed]
9. Tahir, M.; Pan, L.; Idrees, F.; Zhang, X.; Wang, L.; Zou, J.-J.; Wang, Z.L. Electrocatalytic oxygen evolution reaction for energy conversion and storage: A comprehensive review. *Nano Energy* **2017**, *37*, 136–157. [CrossRef]
10. Hu, X.; Wang, Y.; Wu, Q.; Li, J. Review of cobalt-based nanocomposites as electrode for supercapacitor application. *Ionics* **2022**, *28*, 989–1015. [CrossRef]
11. Qiao, X.; Liao, S.; Zheng, R.; Deng, Y.; Song, H.; Du, L. Cobalt and Nitrogen Codoped Graphene with Inserted Carbon Nanospheres as an Efficient Bifunctional Electrocatalyst for Oxygen Reduction and Evolution. *ACS Sustain. Chem. Eng.* **2016**, *4*, 4131–4136. [CrossRef]
12. Wang, Z.; Xiao, S.; Zhu, Z.; Long, X.; Zheng, X.; Lu, X.; Yang, S. Cobalt-Embedded Nitrogen Doped Carbon Nanotubes: A Bifunctional Catalyst for Oxygen Electrode Reactions in a Wide pH Range. *ACS Appl. Mater. Interfaces* **2015**, *7*, 4048–4055. [CrossRef] [PubMed]
13. Dou, S.; Li, X.; Tao, L.; Huo, J.; Wang, S. Cobalt nanoparticle-embedded carbon nanotube/porous carbon hybrid derived from MOF-encapsulated Co$_3$O$_4$ for oxygen electrocatalysis. *Chem. Commun.* **2016**, *52*, 9727–9730. [CrossRef] [PubMed]
14. Li, X.; Zeng, C.; Jiang, J.; Ai, L. Magnetic cobalt nanoparticles embedded in hierarchically porous nitrogen-doped carbon frameworks for highly efficient and well-recyclable catalysis. *J. Mater. Chem. A* **2016**, *4*, 7476–7482. [CrossRef]
15. Naveen, A.N.; Manimaran, P.; Selladurai, S. Cobalt oxide (Co$_3$O$_4$)/graphene nanosheets (GNS) composite prepared by novel route for supercapacitor application. *J. Mater. Sci. Mater. Electron.* **2015**, *26*, 8988–9000. [CrossRef]
16. Lakra, R.; Kumar, R.; Sahoo, P.K.; Sharma, D.; Thatoi, D.; Soam, A. Facile synthesis of cobalt oxide and graphene nanosheets nanocomposite for aqueous supercapacitor application. *Carbon Trends* **2022**, *7*, 100144. [CrossRef]
17. Liu, B.; Jin, L.; Zheng, H.; Yao, H.; Wu, Y.; Lopes, A.; He, J. Ultrafine Co-based Nanoparticle@Mesoporous Carbon Nanospheres toward High-Performance Supercapacitors. *ACS Appl. Mater. Interfaces* **2017**, *9*, 1746–1758. [CrossRef] [PubMed]
18. Yi, M.; Shen, Z. A review on mechanical exfoliation for the scalable production of graphene. *J. Mater. Chem. A* **2015**, *3*, 11700–11715. [CrossRef]
19. Pei, S.; Cheng, H.-M. The reduction of graphene oxide. *Carbon* **2012**, *50*, 3210–3228. [CrossRef]
20. Tetlow, H.; Posthuma de Boer, J.; Ford, I.J.; Vvedensky, D.D.; Coraux, J.; Kantorovich, L. Growth of epitaxial graphene: Theory and experiment. *Phys. Rep.* **2014**, *542*, 195–295. [CrossRef]
21. Mohan, V.B.; Lau, K.; Hui, D.; Bhattacharyya, D. Graphene-based materials and their composites: A review on production, applications and product limitations. *Compos. Part B Eng.* **2018**, *142*, 200–220. [CrossRef]
22. Mbayachi, V.B.; Ndayiragije, E.; Sammani, T.; Taj, S.; Mbuta, E.R.; Khan, A. ullah Graphene synthesis, characterization and its applications: A review. *Results Chem.* **2021**, *3*, 100163. [CrossRef]
23. Kostoglou, N.; Tarat, A.; Walters, I.; Ryzhkov, V.; Tampaxis, C.; Charalambopoulou, G.; Steriotis, T.; Mitterer, C.; Rebholz, C. Few-layer graphene-like flakes derived by plasma treatment: A potential material for hydrogen adsorption and storage. *Microporous Mesoporous Mater.* **2016**, *225*, 482–487. [CrossRef]
24. Natter, N.; Kostoglou, N.; Koczwara, C.; Tampaxis, C.; Steriotis, T.; Gupta, R.; Paris, O.; Rebholz, C.; Mitterer, C. Plasma-Derived Graphene-Based Materials for Water Purification and Energy Storage. *C* **2019**, *5*, 16. [CrossRef]
25. Warren, B.E. X-ray Diffraction in Random Layer Lattices. *Phys. Rev.* **1941**, *59*, 693–698. [CrossRef]
26. Kostoglou, N.; Liao, C.W.; Wang, C.Y.; Kondo, J.N.; Tampaxis, C.; Steriotis, T.; Giannakopoulos, K.; Kontos, A.G.; Hinder, S.; Baker, M.; et al. Effect of Pt nanoparticle decoration on the H2 storage performance of plasma-derived nanoporous graphene. *Carbon* **2021**, *171*, 294–305. [CrossRef]
27. Brunauer, S.; Emmett, P.H.; Teller, E. Adsorption of Gases in Multimolecular Layers. *J. Am. Chem. Soc.* **1938**, *60*, 309–319. [CrossRef]
28. Hausmann, J.N.; Traynor, B.; Myers, R.J.; Driess, M.; Menezes, P.W. The pH of Aqueous NaOH/KOH Solutions: A Critical and Non-trivial Parameter for Electrocatalysis. *ACS Energy Lett.* **2021**, *6*, 3567–3571. [CrossRef]
29. Lee, B.W.; Alsenz, R.; Ignatiev, A.; Van Hove, M.A. Surface structures of the two allotropic phases of cobalt. *Phys. Rev. B* **1978**, *17*, 1510–1520. [CrossRef]

30. Delhaes, P. *Graphite and Precursors*; Delhaes, P., Ed.; Gordon & Breach Science Publishers: Langhorne, PA, USA, 2001; Volume 1, ISBN 9056992287.

31. Cuesta, A.; Dhamelincourt, P.; Laureyns, J.; Martinez-Alonso, A.; Tascón, J.M.D. Raman microprobe studies on carbon materials. *Carbon* **1994**, *32*, 1523–1532. [CrossRef]

32. Ferrari, A.C.; Meyer, J.C.; Scardaci, V.; Casiraghi, C.; Lazzeri, M.; Mauri, F.; Piscanec, S.; Jiang, D.; Novoselov, K.S.; Roth, S.; et al. Raman Spectrum of Graphene and Graphene Layers. *Phys. Rev. Lett.* **2006**, *97*, 187401. [CrossRef] [PubMed]

33. Hadjiev, V.G.; Iliev, M.N.; Vergilov, I. V The Raman spectra of Co_3O_4. *J. Phys. C Solid State Phys.* **1988**, *21*, L199. [CrossRef]

34. Wdowik, U.D.; Parlinski, K. Lattice dynamics of CoO from first principles. *Phys. Rev. B* **2007**, *75*, 104306. [CrossRef]

35. Li, Y.; Qiu, W.; Qin, F.; Fang, H.; Hadjiev, V.G.; Litvinov, D.; Bao, J. Identification of Cobalt Oxides with Raman Scattering and Fourier Transform Infrared Spectroscopy. *J. Phys. Chem. C* **2016**, *120*, 4511–4516. [CrossRef]

36. Cançado, L.G.; Jorio, A.; Ferreira, E.H.M.; Stavale, F.; Achete, C.A.; Capaz, R.B.; Moutinho, M.V.O.; Lombardo, A.; Kulmala, T.S.; Ferrari, A.C. Quantifying Defects in Graphene via Raman Spectroscopy at Different Excitation Energies. *Nano Lett.* **2011**, *11*, 3190–3196. [CrossRef] [PubMed]

37. Rouquerol, J.; Rouquerol, F.; Llewellyn, P.; Maurin, G.; Sing, K. *Adsorption by Powders and Porous Solids: Principles, Methodology and Applications*; Academic Press: Cambridge, MA, USA, 2013; ISBN 0080970362.

38. Thommes, M.; Kaneko, K.; Neimark, A.V.; Olivier, J.P.; Rodriguez-Reinoso, F.; Rouquerol, J.; Sing, K.S.W. Physisorption of gases, with special reference to the evaluation of surface area and pore size distribution (IUPAC Technical Report). *Pure Appl. Chem.* **2015**, *87*, 1051–1069. [CrossRef]

39. Thommes, M.; Cychosz, K.A. Physical adsorption characterization of nanoporous materials: Progress and challenges. *Adsorption* **2014**, *20*, 233–250. [CrossRef]

40. Rybachuk, M.; Bell, J.M. Electronic states of trans-polyacetylene, poly(p-phenylene vinylene) and sp-hybridised carbon species in amorphous hydrogenated carbon probed by resonant Raman scattering. *Carbon* **2009**, *47*, 2481–2490. [CrossRef]

41. McIntyre, N.S.; Johnston, D.D.; Coatsworth, L.L.; Davidson, R.D.; Brown, J.R. X-ray photoelectron spectroscopic studies of thin film oxides of cobalt and molybdenum. *Surf. Interface Anal.* **1990**, *15*, 265–272. [CrossRef]

42. National Institute of Standards and Technology, NIST X-ray Photoelectron Spectroscopy Database (SRD 20), Version 5.0. Available online: https://srdata.nist.gov/xps/ (accessed on 15 February 2024).

43. Vaz, C.A.F.; Prabhakaran, D.; Altman, E.I.; Henrich, V.E. Experimental study of the interfacial cobalt oxide in $Co_3O_4/\alpha-Al_2O_3(0001)$ epitaxial films. *Phys. Rev. B* **2009**, *80*, 155457. [CrossRef]

44. Bajdich, M.; García-Mota, M.; Vojvodic, A.; Nørskov, J.K.; Bell, A.T. Theoretical Investigation of the Activity of Cobalt Oxides for the Electrochemical Oxidation of Water. *J. Am. Chem. Soc.* **2013**, *135*, 13521–13530. [CrossRef] [PubMed]

45. Jia, Q.; Gao, Y.; Li, Y.; Fan, X.; Zhang, F.; Zhang, G.; Peng, W.; Wang, S. Cobalt nanoparticles embedded in N-doped carbon on carbon cloth as free-standing electrodes for electrochemically-assisted catalytic oxidation of phenol and overall water splitting. *Carbon* **2019**, *155*, 287–297. [CrossRef]

46. Fletcher, S. Tafel slopes from first principles. *J. Solid State Electrochem.* **2009**, *13*, 537–549. [CrossRef]

47. Antipin, D.; Risch, M. Calculation of the Tafel slope and reaction order of the oxygen evolution reaction between pH 12 and pH 14 for the adsorbate mechanism. *Electrochem. Sci. Adv.* **2023**, *3*, e2100213. [CrossRef]

48. Mao, S.; Wen, Z.; Huang, T.; Hou, Y.; Chen, J. High-performance bi-functional electrocatalysts of 3D crumpled graphene–cobalt oxide nanohybrids for oxygen reduction and evolution reactions. *Energy Environ. Sci.* **2014**, *7*, 609–616. [CrossRef]

49. Su, Y.; Zhu, Y.; Jiang, H.; Shen, J.; Yang, X.; Zou, W.; Chen, J.; Li, C. Cobalt nanoparticles embedded in N-doped carbon as an efficient bifunctional electrocatalyst for oxygen reduction and evolution reactions. *Nanoscale* **2014**, *6*, 15080–15089. [CrossRef] [PubMed]

50. Lu, C.; Liu, L.; Yang, Y.; Ma, Y.; Luo, Q.; Zhu, M. Recent Progress in Co_3O_4-Based Nanomaterials for Supercapacitors. *ChemNanoMat* **2023**, *9*, e202200537. [CrossRef]

51. Dong, X.-C.; Xu, H.; Wang, X.-W.; Huang, Y.-X.; Chan-Park, M.B.; Zhang, H.; Wang, L.-H.; Huang, W.; Chen, P. 3D Graphene–Cobalt Oxide Electrode for High-Performance Supercapacitor and Enzymeless Glucose Detection. *ACS Nano* **2012**, *6*, 3206–3213. [CrossRef]

52. Yan, J.; Wei, T.; Qiao, W.; Shao, B.; Zhao, Q.; Zhang, L.; Fan, Z. Rapid microwave-assisted synthesis of graphene nanosheet/Co_3O_4 composite for supercapacitors. *Electrochim. Acta* **2010**, *55*, 6973–6978. [CrossRef]

53. Vilian, A.T.E.; Dinesh, B.; Rethinasabapathy, M.; Hwang, S.-K.; Jin, C.-S.; Huh, Y.S.; Han, Y.-K. Hexagonal Co_3O_4 anchored reduced graphene oxide sheets for high-performance supercapacitors and non-enzymatic glucose sensing. *J. Mater. Chem. A* **2018**, *6*, 14367–14379. [CrossRef]